Inner-shell promotions in low-energy Li^+-Al collisions at clean and alkali-covered Al(100) surfaces

K. A. H. German,* C. B. Weare, and J. A. Yarmoff
Department of Physics, University of California, Riverside, California 92521
and Materials Sciences Division, Lawrence Berkeley Laboratory, Berkeley, California 94720
(Received 16 May 1994)

Spectra of scattered ions and ion-induced electron emissions are used to investigate the electronic processes that occur during 0.4–5.0-keV Li^+ bombardment of clean and alkali-atom-covered Al(100). The results show that Li 1*s* electrons are promoted during hard Li-Al collisions, but not during Li-K or Li-Na collisions. Consequences of the inner-shell electron promotions are evident in the inelastic loss, neutralization behavior, and electron emissions of the scattered Li particles. Spectra of scattered Li^+ ions exhibit discrete-loss features, which are resistant to the usual increase in resonant neutralization that accompanies the deposition of alkali atoms on the surface. The loss features are due to Li 1*s* excitation via electron promotion, while the production of ions away from the surface via autoionization is responsible for their lack of response to alkali-atom adsorption. Spectra of ion-induced electron emissions confirm that $Li^*(1s2s^2)$ is produced and that it undergoes autoionization.

I. INTRODUCTION

The interaction of energetic ions with surfaces is a complex process involving many fundamental and often intergrated phenomena. Important electronic aspects of ion-surface collisions include inelastic losses;[1] neutralization and charge exchange;[2,3] excitations of incident ions, target surfaces, and sputtered particles;[4] and ion-induced electron emissions.[5] These processes are important in applications such as ion scattering spectroscopy (ISS), secondary ion mass spectroscopy (SIMS), bombardment-activated chemistry, reactive ion etching, and ion deposition. The present work investigates the inelastic losses, charge exchange, electronic excitations, and electron emissions produced by Li^+ bombardment of clean and alkali-covered Al(100) in the energy regime relevant to low-energy ion scattering spectroscopy (LEIS), i.e., 0.4 to 5.0 keV.

Over the past decade or so, LEIS has become a well-established technique for determining surface geometries.[6,7] LEIS is well suited for structural determinations, not only because its energy and angular distributions are extremely sensitive to surface structure and composition, but also because ion scattering in this energy regime can be described to a high degree of accuracy with relatively simple models based on classical elastic scattering. However, an understanding of the energy loss and neutralization behavior is also crucial to the accurate interpretation of LEIS data. The present system represents a case in which the prevailing models for alkali ion scattering are blatantly inadequate.

Energy losses experienced by ions with incident energies in excess of a few hundred eV are usually modeled by a combination of elastic energy losses due to classical binary scattering from target nuclei and continuous inelastic losses due to the dissipative forces of surface electrons on the moving projectile. The elastic loss is given by the binary collision model (BCM), which treats the ion-surface interaction as a series of independent classical elastic collisions between the ion and unbound target atoms. According to the BCM, the final energy of a projectile with incident energy E_0 and mass m_1, scattered through an angle Ψ, from a target atom with mass m_2 is

$$E_1 = E_0 \left[\frac{\cos\Psi + \sqrt{m_2^2/m_1^2 - \sin^2\Psi}}{(1+m_2/m_1)} \right]^2 . \quad (1)$$

A typical alkali-ion scattering energy spectrum displays a single scattering peak (SSP) for each element present on the surface, as well as both a low-energy tail and a smaller high-energy tail associated with each SSP, which result from multiple scattering. While the continuous inelastic losses are generally much smaller than the elastic losses, they do cause features in scattered ion spectra to broaden and to shift below the BCM energy, an effect which increases with E_0.[1]

It is generally assumed that the ion fraction of scattered alkali ions is accurately described by resonant neutralization.[2] Resonant charge exchange occurs when the outer-shell energy level of a particle located within a few Å's of a surface overlaps the Fermi level, so that electrons can reversibly tunnel between the particle and the surface. Resonant charge exchange is active in the scattering of alkali ions from surfaces because the ionization potentials of alkalis are comparable to the work functions of many materials. Since resonant charge exchange is reversible, it is usually assumed that the survival probability of alkali ions is essentially independent of the ion trajectory for a given ion-surface combination.[8] This is in contrast to the behavior of noble-gas ions, which typically undergo such a high rate of irreversible Auger neutralization that only ions that have singly scattered from the top layer are likely to survive.[9] Therefore, while noble-gas ion scattering can only probe the outermost atomic layer, alkali-ion scattering can probe the structure of the first several atomic layers.[7]

Because the resonant neutralization probability of scattered alkali ions depends strongly on the surface work function, it can be drastically altered by the deposition of even trace amounts of an adsorbate. Several studies have been done to characterize the effects of alkali-atom adsorption on the resonant neutralization of alkali ions scattered from metal surface.[10-19] The most obvious effect is an increase in resonant neutralization, since adsorbed alkali atoms reduce the surface work function via the formation of surface dipoles.[20,21] Several of the studies suggest that, under certain conditions, resonant neutralization may also be influenced by inhomogeneities in the surface local electrostatic potential.[14-17,19] Resonant tunneling can also produce excited neutral atoms and negative ions by populating low-lying valence states.[18]

The present work is a followup of previous experiments investigating Li^+ scattering from clean and alkali-atom-covered Al(100), which were briefly described in two papers.[12,22] There is renewed interest in alkali-atom adsorption on Al surfaces due to recent reports that these systems display some unanticipated adsorption properties. In particular, alkali atoms adsorb at ordered metastable hollow sites when deposited on cooled ($\sim$100 K) single-crystal Al surfaces, and then, when warmed to room temperature, undergo an irreversible ordered intermixing with the first atomic layer of the substrate.[23-32] The ion scattering experiments reported in Ref. 12 were originally undertaken to determine the structure of Na/Al(100), but instead showed that the neutralization of Li^+ ions scattered from these surfaces is highly site specific. In particular, the ion fraction of 3-keV Li^+ ions scattered toward the surface normal from Na/Al(100) is higher for the Al SSP than for the rest of the scattered ion signal. This was demonstrated by monitoring the response of Li^+ ion scattering spectra to Na deposition. While Na deposition produced the expected increase in resonant neutralization for the multiple scattering signal, the intensity of the Al SSP remained high. At the same time, the Na SSP was virtually undetectable, even in cases where Na coverages were high enough to produce comparable amounts of single scattering from Na and Al. The anomalously high ion yield for ions singly scattered from Al sites was interpreted as resulting from an inhomogeneous local electrostatic potential. The next study showed this interpretation to be insufficient.

Results presented in Ref. 22 demonstrated that Li 1*s* electrons are promoted to empty states near the Fermi level during hard Li-Al collisions, as evidenced by a discrete-loss feature associated with the Al SSP. This was an unexpected result, since inner-shell electron promotions have received virtually no attention in the LEIS literature related to alkali-ion scattering. Note that several cases of inelastic losses or changes in neutralization behavior associated with the promotion of the outer-shell electrons of scattered low-energy noble-gas ions have been reported.[33-44] However, the only case of an inelastic loss produced by an inner-shell electron promotion that is known to the authors involves the promotion of Na 2*p* electrons in low-energy Na-Na collision at Na-contaminated Ag surfaces.[45] More information on electron promotions relevant to LEIS can be found in the literature on ion-induced electron emissions, which identify core holes produced during ion-surface collisions by monitoring the emitted Auger electrons.[4,5] In all of the studies of Auger electron emissions produced by low-energy alkali-ion bombardment that are known to the authors, however, core-level electron promotions involving the projectile were only observed for symmetric collisions, i.e., Li-Li,[46,47] Na-Na,[45] and K-K collisions.[48,49]

Perhaps more important to LEIS than inelastic losses associated with electron promotions are the ramifications of electron promotions to the ion survival probability. In the data presented in Ref. 22, the promotion of Li 1*s* electrons changed the neutralization behavior of Li projectiles by initiating the formation of autoionizing states that contributed to the ion yield. The autoionization process was verified by spectra of the ion-induced electron emissions. The identification of autoionizing states in Ref. 22 illuminated the underlying cause of the site-specific neutralization observed in the previous study.[12] For the data collected at 3 keV, nearly all of the signal produced by single scattering from Al was at the loss feature. This was not evident in the first study, as the Al SSP appeared only as a small shoulder on the high-energy side of the loss feature. It was therefore the loss feature intensity that was resistant to the usual increase in neutralization induced by Na adsorption. The reason that the loss feature intensity remained high, in spite of Na deposition, was that the promotions responsible for the inelastic loss produced excited neutrals, which autoionized above the surface and thus augmented the ion fraction of the loss feature. The site-specific neutralization reported in the earlier studies, was, therefore, caused by the selective excitation of Li in Li-Al collisions, as opposed to Li-Na collisions. Experiments are currently in progress that look at the same systems with a time-of-flight analyzer capable of detecting both ions and neutrals. Early results show that, while the effects are not as large as those produced by autoionization, variations in the surface local electrostatic potential do, in fact, contribute to site-specific resonant neutralization.[19]

The present work represents a more in-depth study of the inelastic loss, charge exchange, electronic excitations, and electron emissions relevant to Li^+ bombardment of clean and alkali-atom-covered Al(100) surfaces than previously reported. By employing a larger range of incident energies, sample orientations, scattering angles, and alkali coverages, the spectra of scattered ions and electron emissions reveal several additional intricacies of the effects of Li inner-shell promotions. Monte Carlo simulations of ion scattering spectra are also used to distinguish between spectral characteristics that are produced by elastic and inelastic processes. Experimental procedures are described in Sec. II. Results are presented in Sec. III and are discussed in Sec. IV. Section V summarizes the important results.

II. EXPERIMENTAL PROCEDURE

The Al(100) sample was cut with an electric discharge machine from a single-crystal boule that was oriented by

Laue x-ray diffraction to within 0.25° of the (100) plane. It was then leveled with 600-grit sandpaper and polished with a suspension of MgO. After confirming the orientation, the surface was polished with 0.3-μm diamond paste followed by colloidal silica (Beuhler). Use of the colloidal silica was much simpler and safer than the chemical etch typically employed in the final polishing stage for Al single crystals. The quality of the surface proved to be superior to that of the commercial Al(100) sample used in a previous study,[12] as determined by ion scattering angular distributions.[50]

The sample was mounted on a manipulator (Vacuum Generators) with three transitional and two rotational degrees of freedom, and placed in the ultrahigh-vacuum chamber (base pressure equal to 3×10^{-11} Torr) in which all of the experiments were performed. The vacuum chamber consists of three working levels. The upper level houses a four grid reverse-view low-energy electron diffraction (LEED) system. The LEED optics are also used as a retarding field analyzer (RFA) for Auger electron spectroscopy (AES). The middle level contains a $^7Li^+$ ion gun (Kimball Physics), an electron gun, a sputter gun, and an electrostatic analyzer (ESA) based on a double-focusing 160° spherical sector (Comstock). The lower level is used for evaporations.

In-vacuum sample preparation consisted of reiteratively sputtering with grazing incidence 2-keV Ar^+ and normal incidence 0.5-keV Ar^+, and annealing to approximately 420°C for a minimum of 20 min. The purity and order of the surface were verified with AES and LEED. Polar angle scans of singly scattered $^7Li^+$ ions, which are more sensitive to surface order than LEED,[50] were used as a final measure of surface quality. All K and Na depositions and ion scattering measurements were performed at room temperature. Well-outgassed SAES getters were used for Na and K deposition. AES spectra taken before and after data collection verified that O contamination remained at $<0.1\%$ ML, where 1 ML is defined as the number of atoms in a single bulk-terminated Al(100) layer.

Calibration of K coverages was performed by comparing the alkali-induced change in work function, $\Delta\phi$, to those published in Ref. 51 for K/Al(100). $\Delta\phi$ was determined by measuring the shift in the low-energy cutoff of the secondary electrons that were produced by a 200-eV electron beam incident on the sample in a direction 57° from the surface normal and emitted along the normal. Electron cutoff spectra were collected immediately before and after depositions, with the sample biased at -20 V to lift the cutoff above any low-energy electrons produced by filaments. AES intensity ratios of the K 252-eV peak to the Al 68-eV peak are also reported as raw intensities uncorrected for elemental sensitivities or for the energy dependence of the RFA analyzer response. Coverages of Na-covered surfaces were calibrated using LEED. The 0.5-ML coverage was determined via a bright and sharp Na/Al(100)-$c(2\times2)$ LEED pattern. The smaller coverages were then assigned by assuming that coverage is proportional to exposure time for coverages below 0.5 ML.

Alkali-covered surfaces were also monitored with He^+ ion scattering using a normal incidence 2-keV He^+ beam and a scattering angle of $\Psi=158°$. It was found that the ratio of the adsorbate SSP to the Al SSP increased monotonically with, and was very sensitive to, the coverage. Therefore, although there is no easy way to determine accurately absolute coverages from He^+ spectra, they did provide an excellent test of the reproducibility of the deposition.

Spectra of scattered Li^+ ions and of ion-induced electron emissions were obtained by targeting samples with 0.4- to 5.0-keV $^7Li^+$ ions, and collecting the scattered ions or emitted electrons with the ESA. By pointing the $^7Li^+$ ion gun directly at the ESA, the energy spread of the incident beam was found to be $<0.2\%$. It was necessary to install a 1-mm-diam aperture 9 cm in front of the $^7Li^+$ ion gun to get a well-collimated beam at lower energies. A Faraday cup was used to profile the ion beam at the sample position. The spot size was ≤1 mm in diameter over the entire energy range. The analyzer resolution was scaled to 1% of the beam energy for the ion scattering spectra. Spectra were collected with two different angles between the ion gun and the analyzer. Most of the data were collected with the analyzer positioned 12° from the $^7Li^+$ ion gun, which gives a scattering angle of $\Psi=168°$. Data were also collected with the analyzer positioned 138° from the ion gun, i.e., $\Psi=42°$. The angular acceptance was $\pm2°$ in both cases. Secondary electron cutoffs were collected with the ESA resolution set to 0.6 eV, while spectra of electron emissions in the energy range of 40–80 eV were collected with the resolution set to 3 eV in order to increase the throughput.

Because ion scattering is a destructive technique, several precautions were taken to ensure that beam damage did not affect the results. First, the entire face of the sample was systematically charted with LEED, using the micrometers on the manipulator as a coordinate system. Only portions of the sample that produced sharp, bright, and undistorted LEED patterns were used. The coordinates of the usable region were translated to the ion scattering level by mapping the perimeter of the sample with the ion beam. The ion flux was then reduced so that several scans taken from a single spot were indistinguishable. Spectra collected by ramping the detection energy in opposite directions were also indistinguishable. To get a reasonable signal-to-noise level, spectra were collected from several different spots and signal averaged. Typically, about 15 spectra were collected from a single prepared surface, with only every other 1 mm^2 of the high-quality surface being used before repreparing the sample.

III. RESULTS

A. Ion scattering spectra from clean Al(100)

The spectra shown in Fig. 1 are of normally incident $^7Li^+$ ions scattered from Al(100) through an angle of $\Psi=168°$ along the [011] azimuth. Each spectrum corresponds to a different E_0 ranging from 0.4 to 5.0 keV, as indicated. The spectra were normalized to equal maximum intensities, with consecutive spectra displaced by the distance indicated by the vertical axis tick marks. The energy scale is set to zero at the BCM energy for sin-

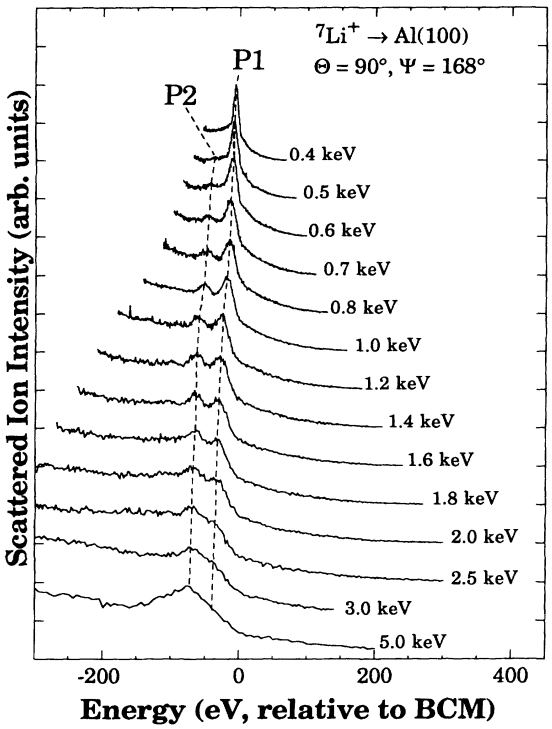

FIG. 1. Spectra of normally incident $^7Li^+$ ions scattered through $\Psi = 168°$ along the [011] azimuth from clean Al(100) for the incident energies indicated. The spectra are normalized to equal peak heights, with consecutive spectra displaced by the distance indicated by the tick marks on the vertical axes.

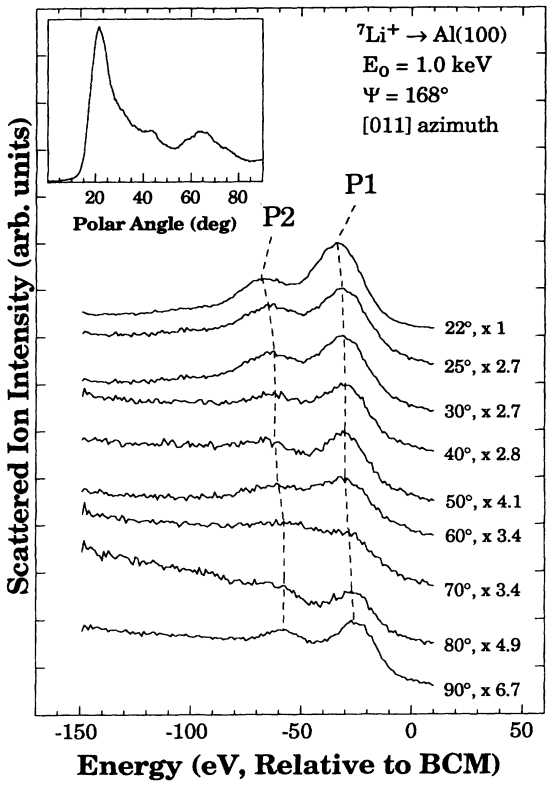

FIG. 2. Spectra of 1-keV $^7Li^+$ ions scattered through $\Psi = 168°$ along the [011] azimuth from clean Al(100) for incident polar angles ranging from $\Theta = 22°$ to 90°. Each spectrum is shifted as in Fig. 1. The inset shows a polar angle scan of the $^7Li^+$ ions scattered through $\Psi = 168°$ along the [011] azimuth at the P1 energy.

gle scattering of ^7Li from ^{27}Al.

Several of the spectra in Fig. 1 display an unanticipated feature. Instead of only one peak, there are two peaks, labeled P1 and P2, evident in most of the spectra. The higher-energy peak, P1, is the only feature visible at the lowest E_0, and is therefore attributed to the usual single scattering from Al. The lower-energy peak, P2, emerges with increasing E_0, and eventually dominates the spectra. The energy separation between P1 and P2, ΔE_{1-2}, remains fairly constant at ~35 eV. As expected, both features broaden and shift further away from the BCM energy with increasing E_0 due to the continuous inelastic losses.

The spectra shown in Fig. 2 were produced by scattering 1-keV $^7Li^+$ ions through a fixed scattering angle of $\Psi = 168°$ from Al(100) along the [011] azimuth at several different incident polar angles, ranging from $\Theta = 22°$ to 90°, where $\Theta = 90°$ is normal incidence. Each spectrum is vertically shifted, as in Fig. 1, and relative scaling factors are indicated. While the absolute intensities of P1 and P2 change significantly with Θ, both peaks are visible in each spectrum. Moreover, their relative positions and intensities are essentially unchanged over the entire range of incident angles. The same result was found for scattering along the [001] azimuth. The large changes in shape and intensity of the spectra are expected, as the effects of focusing and channeling vary with the crystal orientation.[6] This is demonstrated in the inset, which shows a polar angle scan of the scattered ion intensity at P1 taken along the [011] azimuth. Note that the first peak in the polar angle scan, at ~22°, is the surface flux peak (SFP), which is produced by surface atoms focusing ion flux onto adjacent atoms in the same layer.

In an effort to see how P2 is affected by the scattering angle, spectra were also collected for $^7Li^+$ scattering from Al(100) through an angle of $\Psi = 42°$. As seen in Fig. 3, these spectra have complex shapes, but there are no obvious peaks analogous to P1 and P2. Note that the peaks in these spectra are substantially broader than those in Figs. 1 and 2. This is due primarily to the many multiple glancing-angle collisions that have a final energy at or near the SSP energy.

B. Ion scattering spectra from alkali-covered Al(100)

The relative intensities of P1 and P2 respond dramatically to the deposition of alkali atoms on the sample. The spectra shown in Fig. 4 were taken under the same conditions as the spectra in Fig. 1, except that 0.24 ML of K was first deposited on the surface. This K deposition produces a work-function shift of $\Delta\phi = -1.9$ eV and a K 254 eV to Al 68 eV AES ratio of 0.027. The factors on the right of Fig. 4 indicate the decrease in the maximum intensity as compared to the spectra collected from the

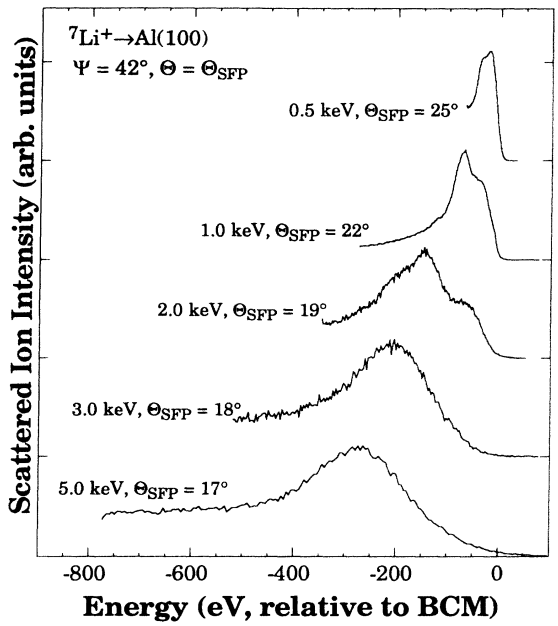

FIG. 3. Spectra of $^7Li^+$ ions scattered from Al(100) in the [011] plane through $\Psi = 42°$. The ion beam is incident along $\Theta = \Theta_{SFP}$ for each E_0, as indicted. Spectra are normalized and shifted as in Fig. 1.

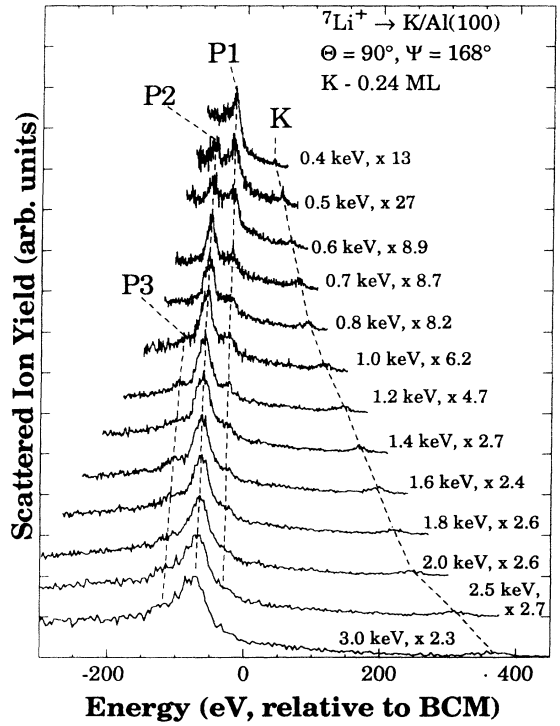

FIG. 4. Spectra of normally incident $^7Li^+$ ions scattered through $\Psi = 168°$ along the [011] azimuth from Al(100) with a 0.24-ML K coverage Incident energies and scaling factors relative to the corresponding spectra in Fig. 1 are indicated. The spectra are displayed by the distance indicated by the tick marks on the vertical axes.

clean surface. The correlation of higher factors with lower E_0 reflects a greater degree of alkali adsorbate-induced resonant neutralization at lower projectile velocities.

In addition to the peaks P1 and P2, which are evident in the data collected from the clean surface, there are two other discernible peaks, labeled K and P3, in the spectra shown in Fig. 4. Although these peaks are small, and may be somewhat difficult to discern in any single spectrum, they are evident as subtle, but persistent, features in the spectra collected at different incident energies. The peak labeled K, located at higher energies, is readily identified as the K SSP. The peak labeled P3, on the other hand, is not so easily identified. Some interesting characteristics of P3 are that it has an onset at about $E_0 = 1.0$ keV and is located below P2 and P1, with the separation between P1 and P3, ΔE_{1-3}, remaining fairly constant at ~ 80 eV. P3 is actually visible in some of the clean surface spectra (see Fig. 1), but is even more difficult to distinguish above the higher background. Note that the intensities of P2 and P3 are not as affected by K adsorption as are P1 and the multiple scattering background.

The evolution of the scattered Li^+ spectra as a function of alkali-atom coverage is shown in Fig. 5 for (a) 1.0-keV, (b) 3.0-keV, and (c) 5.0-keV normal incidence $^7Li^+$ beams. In all cases, the multiple scattering background decreases precipitously with alkali coverage, while the P2 and P3 signals remain strong. In Fig. 5(a), where $E_0 = 1.0$ keV, P1 and P2 are well separated, and P1 decreases much more rapidly with alkali coverage than does P2. P1, P2, and P3 are all present, although somewhat difficult to distinguish, in Fig. 5(b), where $E_0 = 3.0$ keV. The shape of the overall single scattering signal, however, clearly does change with alkali-atom coverage. As more Na is deposited, the shoulder corresponding to P1 disappears, and P3 becomes more evident as the background decreases. In Fig. 5(c), where $E_0 = 5.0$ keV, P2 is the dominant feature and P1 is not visible, although P3 is seen as a shoulder on the low-energy side of P2, even for the spectra collected from the clean surface. Note that single scattering from either Na or K is very weak in all cases.

As a cross reference, 2-keV He^+ ion scattering spectra collected from some of the same surfaces are shown in Fig. 6. The He^+ spectra do not exhibit a significant multiple scattering background because virtually all of the multiply scattered He^+ ions undergo Auger neutralization. In contrast to the scattered Li^+ spectra, single scattering peaks associated with the alkali adsorbates are many times more prominent in the He^+ spectra. For example, the K SSP is much larger than the Al SSP in the He^+ ion scattering spectra than it is in the Li^+ ion scattering spectra (see Fig. 4). Likewise, while the Na SSP is larger than the Al SSP in the He^+ scattering data collected from surfaces with a 0.5-ML coverage, a Na SSP is barely discernible in the corresponding Li^+ spectra shown in Figs. 5(b) and 5(c).

To better characterize the evolution of the $^7Li^+$ ion scattering spectra as a function of E_0, peaks in the normal incidence data of Figs. 1 and 4 were fit to Gaussian

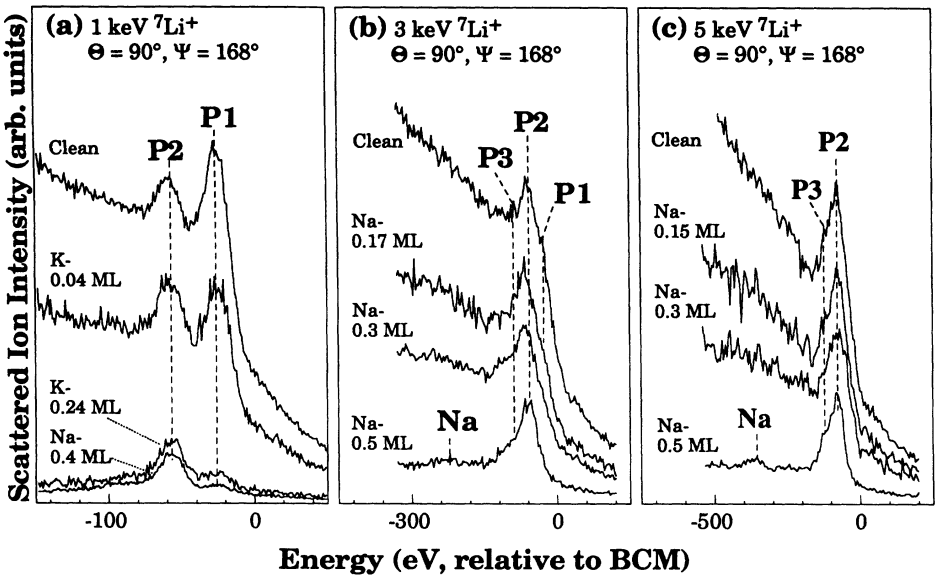

FIG. 5. Spectra of normally incident $^7Li^+$ ions scattered through $\Psi = 168°$ along the [011] azimuth from Al(100) surfaces with various alkali coverages for E_0 = (a) 1.0, (b) 3.0, and (c) 5.0 keV. The work-function changes associated with the K-0.04 ML and K-025 ML coverages are $\Delta\phi = -0.6$ and 1.9 eV, respectively. The expected position of the Na SSP is indicated in (b) and (c).

line shapes after removing the multiple scattering background. While there is some ambiguity in separating the background from the single scattering signal, the Monte Carlo simulations, described below, gave the approximate shape of the background. The background was simulated by a spline function and then removed from the data. To test the uncertainty introduced by the background subtraction, several fits were performed with different choices for the background shape. The idea that the positions, widths, and intensities of the peaks, as well as the shape of the background, should all evolve gradually as a function of energy was also a helpful guiding principle in fitting the data.

Peak positions determined by this procedure are plotted in Fig. 7 as a function of E_0. The locations of P1, P2, and P3 are given with respect to the BCM for a ^{27}Al target atom, while the K SSP position is given with respect to the BCM for a ^{39}K target atom. At lower energies, where the peaks are narrow and have intensities well above the background, the accuracy of the fits was within ± 1 eV. At higher energies, the accuracy degraded as scattering from deeper layers increased the relative intensity of the background with respect to the peaks, and as the peaks broadened due to the increased continuous inelastic energy losses.

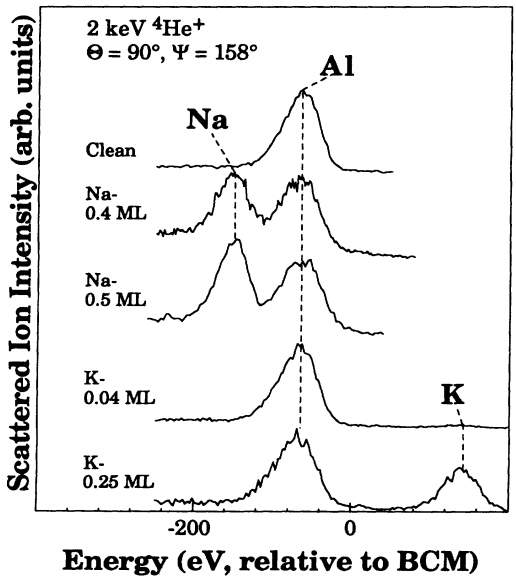

FIG. 6. Spectra of normally incident $^4He^+$ ions scattered through $\Psi = 158°$ along the [011] azimuth from Al(100) with various alkali coverages, as indicated.

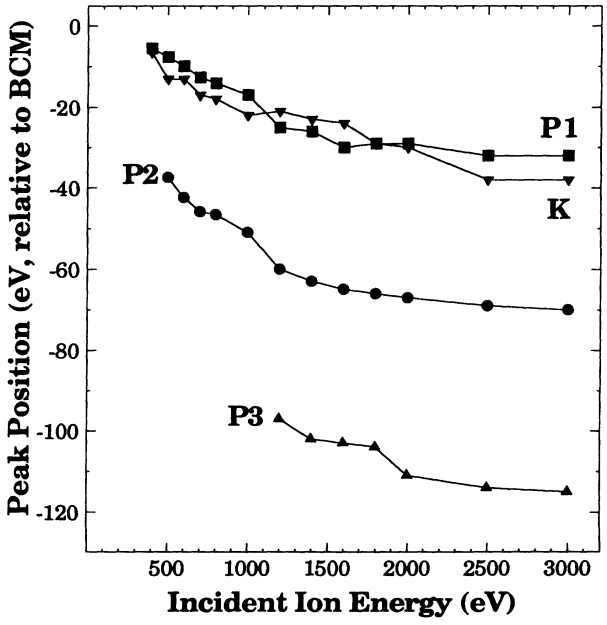

FIG. 7. The locations of P1, P2, and P3 as a function of E_0 given with respect to the BCM for scattering from an ^{27}Al target atom, and the location of the K SSP given with respect to the BCM for a ^{39}K target atom.

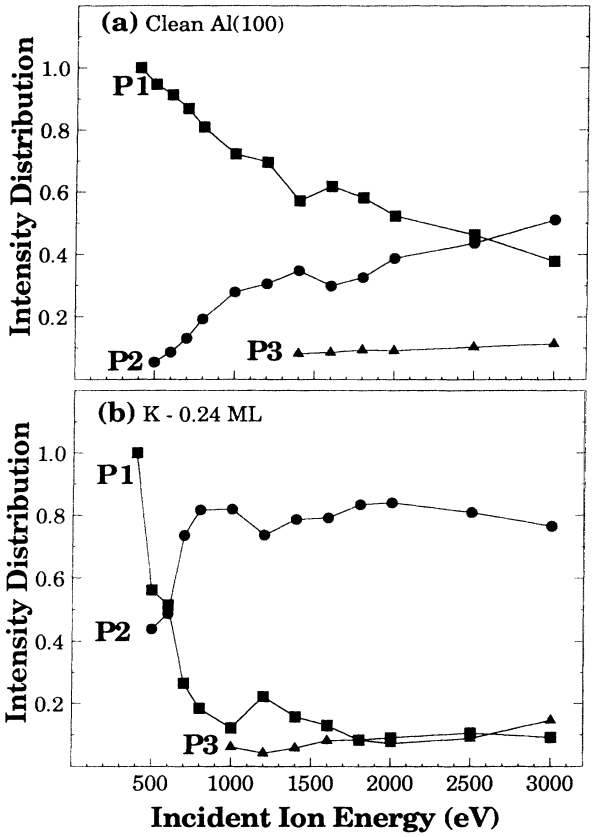

FIG. 8. The intensities of P1, P2, and P3, normalized to the sum of the intensities, as a function of E_0 for spectra collected from (a) clean Al(100) and (b) Al(100) with 0.24 ML of K.

The fractional intensities of P1, P2, and P3, i.e., Px/(P1 + P2 + P3), are shown in Fig. 8 as a function of E_0 for spectra collected from (a) the clean surface, and (b) a surface with 0.24 ML of K. In the spectra collected from the clean surface, there is a gradual shift in intensity from P1 to P2 as E_0 increases, until P2 overtakes P1. The shift is, however, much more dramatic for the K-covered surface, where P2 goes from being nonexistent to being the dominant peak over a 300-eV interval in E_0.

C. Spectra of ion-induced electron emissions

Spectra of the electron emissions produced by a $^7Li^+$ beam impinging on Al(100) were collected to look for evidence of core-level excitations. Peaks in the electron emission spectra are due to Auger deexcitation of core-level holes, where the peak energy is indicative of the excited species and the specific de-excitation channel producing the ejected electrons. While this is similar to AES, which employs an electron beam to excite core-level electrons, there are some important differences in ion-induced Auger electron emissions. Ion bombardment can generate excited states both within the incident particles and in the target. Excitations may be produced during collisions involving incident ions or may result from the ensuing collision cascade. Collisions subsequent to an excitation can also open new deexcitation channels involving level crossings.[52] Auger electrons may be emitted from the solid, or from scattered or sputtered particles. Excited neutrals that deexcite via in intra-atomic Auger decay are said to have autoionized. Because the scattered particles are moving, electrons ejected from these sources can also be Doppler shifted by several eV.[4,5]

Spectra of electron emissions produced by bombarding Al(100) with $^7Li^+$ ions were collected for several incident energies. Spectra shown in Fig. 9(a) were collected with the detector at the surface normal, i.e., $\Theta_{det}=90°$, and with the incident ion beam located at $\Theta=78°$ along the [011] azimuth. For the electron emission spectra shown in Fig. 9(b), $\Theta_{det}=\Theta+138°$, i.e., the ion gun and the analyzer are 138° apart, while the incident ion beam is located along the [011] azimuth at either $\Theta=30°$ or $\Theta=\Theta_{SFP}$, as indicated. In Fig. 9, the measured secondary electron cutoff is set to zero so that the energy scale is with respect to the surface vacuum level. Each spectrum was normalized to the ion beam flux, and then scaled by the indicated relative factors. The scaling factors in Fig. 9(b) should not be compared to those in Fig. 9(a), however, as it was not possible to determine the rela-

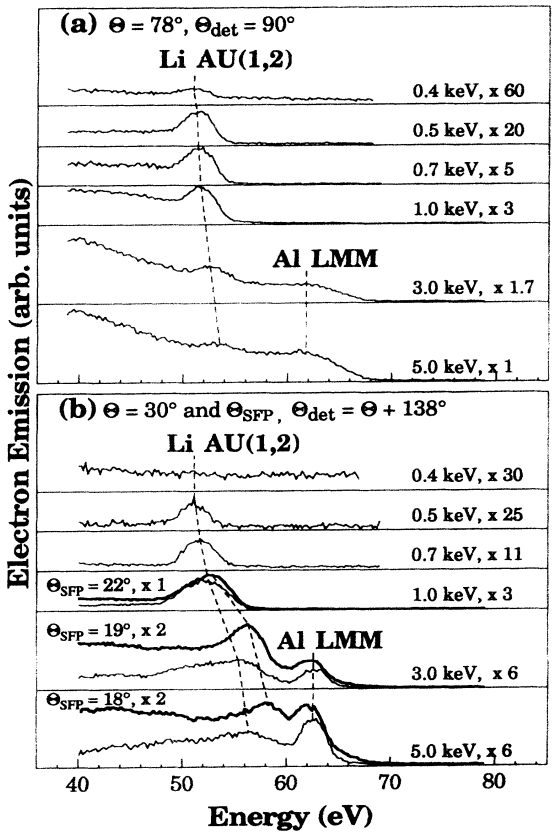

FIG. 9. Energy spectra of the electron emissions produced by $^7Li^+$ ion bombardment collected (a) along the surface normal ($\Theta_{det}=90°$) for ion-beam incidence along $\Theta=78°$ and (b) 138° from the ion-beam incidence direction for $\Theta=30°$ (thin line) and $\Theta=\Theta_{SFP}$ (bold line). Incident energies and scaling factors are indicated.

tive collection efficiency of the analyzer between the two configurations.

Two features are evident in these spectra. The peak at lower energy, marked Li AU(1,2), is attributed to the autoionization of $Li^*(1s2s^2)$, as discussed in Sec. IV. The second peak is due to electrons emitted from Al LMM Auger transitions. The shifts in the Li AU(1,2) peak with E_0 are Doppler shifts, indicating that the Li AU(1,2) signal originates from moving sources. The Doppler shifts provide information about the $Li^*(1s2s^2)$ population, and are discussed below.

The Al LMM peaks change widths in response to changes in the experimental configuration because the Al LMM signal is composed of two components, one broad and one narrow, which have different angular distributions.[53] The narrow component is assigned to the Auger deexcitation of sputtered Al atoms containing $2p$ vacancies, which emit electrons isotopically. The broad component is due to electrons ejected during Auger deexcitations of $2p$ holes in the solid. These electrons are emitted with an approximate cosine distribution about the surface normal, as they are more likely to inelastically scatter before escaping the solid if they are traveling parallel to the surface. This explains why the broad component is prominent in Fig. 9(a) when $\Theta_{det}=90°$, and the narrow component is well isolated in the $\Theta=30°$ spectra shown in Fig. 9(b) when the detector is only 12° above the surface plane. The spectra collected with intermediate Θ_{det}, i.e., when $\Theta=\Theta_{SFP}$, are composed mostly of the atomic component, but also have a small contribution from the solid component. The relative intensities of the atomic and solid Al LMM emissions are also affected by the direction of the incident beam. In particular, since normally incident ions and the collision cascades they initiate are directed into the crystal, a normal incidence beam will create more Al $2p$ holes in the bulk than a grazing incidence beam.

Note that the sharp Al LMM peak can be used to cross check the energy calibration of the present electron emission spectra. In Ref. 53, the narrow peak is located at ~ 67.5 eV with respect to the Al Fermi level. To locate the narrow Al LMM component with respect to the Al(100) vacuum level, the 4.41-eV Al(100) work function must be subtracted, which places it at ~ 63 eV, in excellent agreement with the value measured here.

IV. DISCUSSION

The present results reveal that the interaction of low-energy Li^+ ions with Al(100) and alkali-atom-covered Al(100) cannot be understood within the context of classical scattering and resonant neutralization. In particular, the peaks below the Al SSP and their distinct response to alkali adsorption cannot be accounted for without considering inner-shell electronic excitations and autoionization. As will be seen, the electron emission features indicate that the promotion of Li $1s$ electrons is at the root of the underlying complexity of this system.

It can be concluded that P2 and P3 do not result from classical elastic scattering because it can be shown that they are not produced by contaminants nor are they due to multiple scattering. As seen from Eq. (1), the energy separation between SSP's for two different target masses will roughly scale with E_0. This type of behavior is evident in Fig. 4, where the separation between the Al SSP and the K SSP increases with E_0. By comparison, ΔE_{1-2} and ΔE_{1-3} are fairly insensitive to E_0. Multiple scattering can also be dismissed as an explanation for P2 and P3. The probability for incident ions to undergo a specific scattering sequence is extremely sensitive to scattering conditions. Spectral features resulting from multiple scattering will, therefore, change drastically with sample orientation. In contrast, the spectra in Fig. 2 show that the relative intensities and positions of P2 and P1 are largely unaffected by radical changes in the sample orientation. The persistence of P2, regardless of the geometry of the lattice about the target atom, shows that the underlying mechanism responsible for P2 is highly localized in nature.

Since P2 and P3 cannot be understood within the context of classical scattering, Monte Carlo simulations were performed to help differentiate the elastic and inelastic effects in the experimental data. The simulations, which are described in Ref. 54, model the scattering as a sequence of binary collisions in which the Thomas-Fermi-Molière potential, with the screening length modified by a factor of $c=0.8$, is used to determine the scattering angle as a function of impact parameter. For the results shown in Fig. 10, lattice vibrations with surface enhancements were included, but inelastic losses were not. To improve statistics, acceptance angles in the simulations shown in Figs. 10(a), 10(b), and 10(d) were $\pm 10°$ about the exit angle, rather than $\pm 2°$ as in the experiment. A side effect of increasing the acceptance angle is to broaden the peaks in the simulation. The simulation results are divided into surface events (gray) and subsurface events (white), according to whether or not the trajectory extended past the first two atomic layers, which are the only layers directly visible to the incident ion beam for both normal incidence and at the SFP. Experimental data corresponding to each simulation are superimposed on the figures. Note that features in the experimental spectra are located at lower energies than the corresponding features in the simulations due to the continuous inelastic losses. These continuous losses also act to broaden the features, although this is not evident in all of the spectra due to the use of a larger acceptance angle in some of the simulations.

Figures 10(a) and 10(b) show simulations of experimental data that display both a strong P1 and P2 signal. The scattering parameters are (a) $E_0=1$ keV, $\Psi=168°$, $\Theta=90°$, and (b) $E_0=1$ keV, $\Psi=168°$, $\Theta=22°$. These simulations produced spectra with only one peak, even though the corresponding experimental spectra contain two peaks. All other simulations using $\Psi=168°$ produced only a single peak as well. This confirms that the extra peaks seen in the spectra of scattered ions collected at $\Psi=168°$ are not produced by elastic scattering, and therefore must be the result of discrete inelastic losses associated with single scattering.

Figures 10(c) and 10(d) show examples of how elastic scattering can produce multiple peaks. These Monte Carlo simulations correspond to the spectra shown in

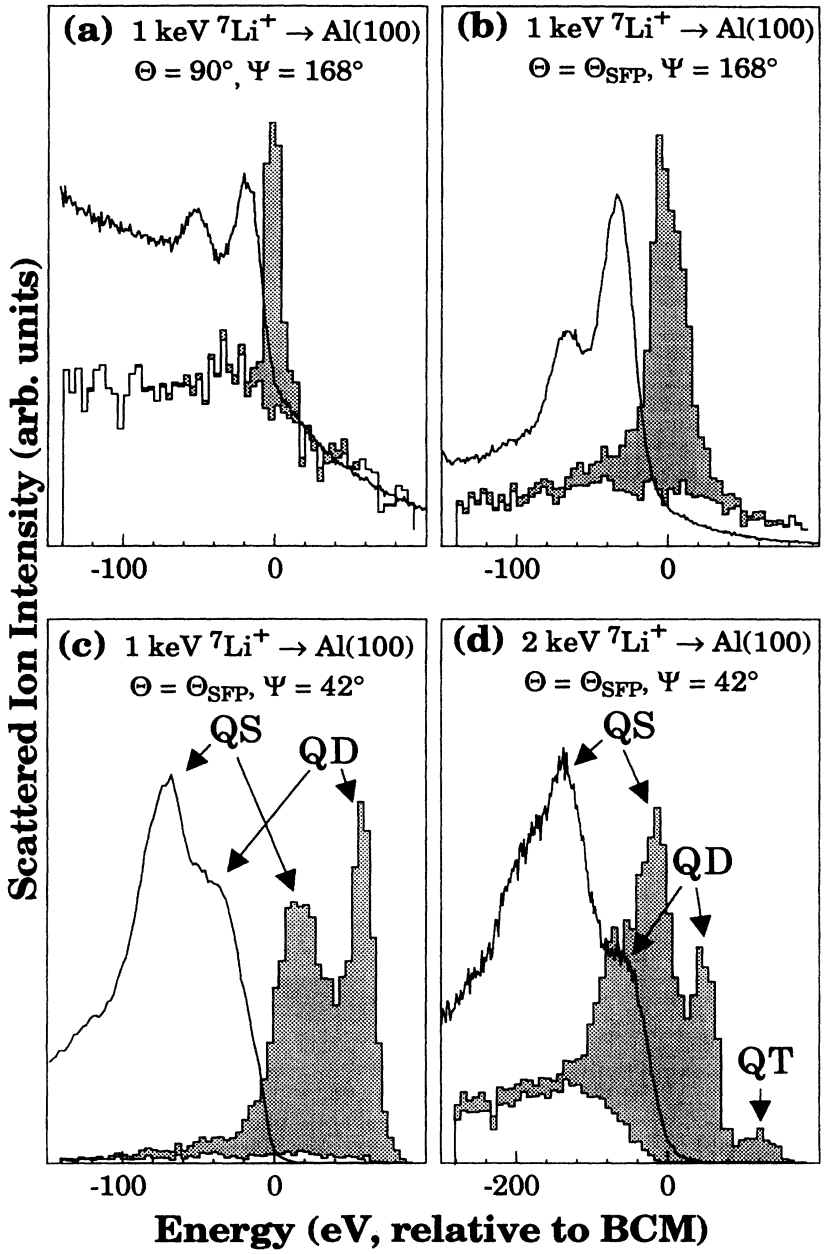

FIG. 10. Monte Carlo simulations of $^7Li^+$ ion scattering spectra for (a) $E_0=1$ keV, $\Psi=168°$, $\Theta=90°$; (b) $E_0=1$ keV, $\Psi=168°$, $\Theta=\Theta_{SFP}=22°$, (c) $E_0=1$ keV, $\Psi=42°$, and $\Theta=\Theta_{SFP}=22°$, and (d) $E_0=2$ keV, $\Psi=42°$, and $\Theta=\Theta_{SFP}=19°$. The histograms are divided into surface events (gray) and subsurface events (white), according to whether or not the trajectory extended past the first two atomic layers. The corresponding experimental data are superimposed on each panel. The intensities of the simulation and the experimental data are arbitrarily scaled to each other.

Fig. 3 for which $E_0=1$ keV, $\Psi=42°$, and $\Theta=\Theta_{SFP}=22°$, and $E_0=2$ keV, $\Psi=42°$, and $\Theta=\Theta_{SFP}=19°$, respectively. For these conditions, both the simulated and the experimental data show a number of peaks, some of which correspond to quasi-single (QS), quasi-double (QD), and quasi-triple (QT) events.[54] QD and QT peaks are due to multiple grazing-angle scattering from two and three neighboring surface atoms, respectively, which readily occurs at small scattering angles. Note that in Fig. 10(c), the relative peak heights of the QS and QD peaks are not the same in the experimental data and the simulation. This is largely due to the broadening that occurs as a consequence of the continuous inelastic losses, which are not accounted for in the simulations. Since the ions involved in a QD trajectory spend more time in the vicinity of the surface, they will experience more inelastic losses than QS ions. Thus, the experimental QD peak is broadened more than the QS. If the relative areas of the QS and QD peaks are considered instead, then the experiment and simulation are well matched. In Fig. 10(d), the general shape of the spectra is consistent between experiment and simulation, and the simulation even reproduces the feature that is located ~50 eV below the QS peak.

The separation of the simulated signal into surface and subsurface events helps to clarify several characteristics of the experimental spectra. The subsurface signal in Fig. 10(a) comprises virtually all of the signal in the high- and low-energy tails. The intensity of the subsurface signal also makes a smooth transition between the high- and low-energy tails underneath the Al SSP. Since the sub-

surface is not directly visible to the incoming beam, this part of the spectrum is not a part of the single scattering intensity. Recall that the general shape of this subsurface signal was used as a guide to determine the shape of the multiple scattering background in fitting the experimental data. In Figs. 10(b), 10(c), and 10(d), there are relatively few subsurface events as compared to Fig. 10(a). This confirms that a Li^+ beam is much less penetrating for incidence at $\Theta=\Theta_{SFP}$ than for $\Theta=90°$. Note that, in Figs. 10(c) and 10(d), the QD and QT peaks are produced by scattering within the first two layers, which is consistent with multiple grazing-angle collisions being prevalent in this configuration.

Given that P2 and P3 cannot be explained within the context of classical scattering, the most logical explanation is that they are loss features due to discrete electronic excitations. Discrete inelastic losses of the magnitude seen here can occur when electrons are promoted to empty states during a binary collision. Electron promotions take place when an occupied level crosses an unoccupied, or partially occupied, level during the collision. Electron promotions are different from resonant charge exchange in that the energy difference between the initial and final states can be several tens of eV's. The level bending necessary to induce such large shifts typically requires internuclear distances of <1 Å. Because the promotion energy is coverted from the kinetic energy of the colliding atoms, electron promotions are associated with discrete inelastic energy losses. Electron promotions can be detected in LEIS by measuring a discrete-loss feature[22,39–42] or an abrupt shift of the SSP to lower energy as a function of either E_0 (Ref. 44) or of the final charge state.[43]

Electron promotions at surfaces have been successfully modeled using a quasimolecular approach developed for binary collisions of isolated atoms, as described in Ref. 55. In the quasimolecular model, the energy levels of the colliding atoms are treated as molecular-orbital (MO) levels which shift as a function of interatomic distance. The evolution of the MO's conform to two limiting cases. At infinite separation, the MO level reduce to the atomic orbitals of the two separate atoms involved in the collision. As the interatomic distance approaches zero, the MO orbitals evolve toward the atomic orbitals of a united atom having the combined nuclear charge of the two separate atoms. At small interatomic distances, it is possible for MO levels to cross. If levels with the same bond symmetry cross, and if one of the levels is not fully occupied, then electrons can be promoted during the level crossing. The relevant parameter in the MO model for determining the onset of a promotion for a given incident energy and scattering angle is the distance of closest approach, which must be within a certain critical distance r_c before a promotion will occur, where r_c is typically between 0.1 and 1.0 Å.

Although the quasimolecular model was developed for isolated atomic binary collisions, it can provide valuable information about the evolution of electronic energy levels during hard binary collisions in a solid. The atomic correlation diagrams shown in Fig. 11 were constructed according to the rules prescribed in Ref. 55. The diagram for Li-Al collisions [Fig. 11(a)] shows that the Li 1*s* level crosses the partially occupied Al 3*p* level, thus allowing Li 1*s* to Al 3*p* electron promotions. For Li-Na collisions, Fig. 11(b) shows that there are no Li 1*s* level crossings, and hence no Li 1*s* promotions are allowed. In the correlation diagram for Li-K collisions (Fig. 11(c)], only fully occupied levels cross the Li 1*s* level, and again Li 1*s* electrons cannot be promoted. If the quasimolecular formalism is relevant, then it is possible for quasimolecular states to mediate Li 1*s* electron promotions during Li-Al collisions, but not during Li-K or Li-Na collisions.

While quasimolecular states mediate the promotion process, the final state of a promoted Li 1*s* electron is not the atomic Al 3*p* level, but rather an empty state of the solid, i.e., a state just above the Fermi level. Since Li 2*s* is in resonance with the Fermi level, the promotion energies are equal to the excitation energies of Li 1*s* electrons to the Li 2*s* level, which requires ~ 59 eV (Ref. 56) for a single excitation, while an excitation involving both Li 1*s* electrons requires 142 eV.[57]

The peak separations ΔE_{1-2} and ΔE_{1-3}, are plotted in Fig. 12 as a function of E_0 and tend to cluster at about 35 and 80 eV, respectively. At first, it may seem that the magnitudes of ΔE_{1-2} and ΔE_{1-3} are inconsistent with the energy required to promote Li 1*s* electrons to the Fermi level. However, the energy lost by a rebounding projectile does not necessarily represent the total excitation energy. Because the mass of ^{7}Li is a non-negligible fraction of the total mass of the ^{7}Li-^{27}Al system, a substantial fraction of the excitation energy, E^*, is absorbed by the recoiling Al atom. Thus, the discrete inelastic loss experienced by the projectile, Q_p, is only a fraction of E^*. Because a promotion occurs during what is essentially a binary atomic collision, the collision can be described using classical equations for a partially inelastic binary collision in which E^* of kinetic energy is removed from the system. Using conservation of energy and momentum, E^* is estimated for a given Q_p as

$$E^*=E_0\left[1-\frac{m_1}{m_2}\right]-E_f\left[1+\frac{m_1}{m_2}\right]+2\frac{m_1}{m_2}\sqrt{E_0E_f}\cos\Psi\ , \tag{2}$$

where $E_f=E_1-Q_p$ and E_1 is given by Eq. (1). Solving Eq. (2) for Q_p gives

$$Q_p=E_1-\left[\frac{\sqrt{E_0}\frac{m_1}{m_2}\cos\Psi+\left\{E^*\left[1+\frac{m_1}{m_2}\right]+E_0\left[1-\left[\frac{m_1}{m_2}\right]^2\sin^2\Psi\right]\right\}^{1/2}}{\left[1+\frac{m_1}{m_2}\right]}\right]^2 . \tag{3}$$

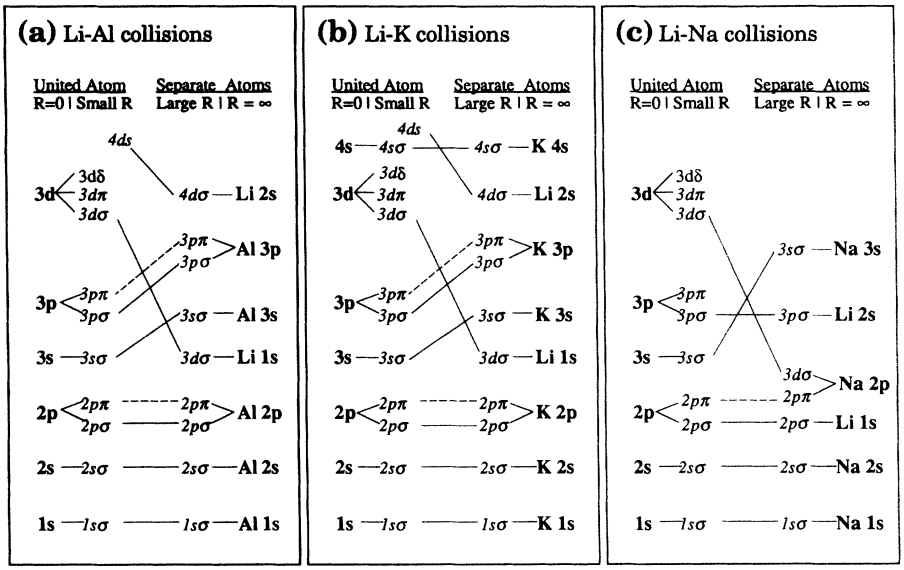

FIG. 11. Atomic correlation diagrams for (a) Li-Al collisions, (b) Li-Na collisions, and (c) Li-K collisions.

Equation (3) can be used to model ΔE_{1-2} and ΔE_{1-3} as a function of E_0 for the present data, where E^* is used as a fitting parameter. This model assumes that extraneous inelastic losses that occur prior to the collision are small compared to E_0, and that the energy losses occurring after the collision do not depend on whether or not the collision was elastic. The contours plotted in Fig. 12 were produced by applying Eq. (3) to the present system. Comparing calculated values of Q_p to ΔE_{1-2} shows that E^*_{1-2} is ~ 60 eV, which is significantly larger than ΔE_{1-2}. To illustrate the response of Q_p to E^*, dashed contours are also plotted for $E^* = 55$ and 65 eV. The best match to the data for ΔE_{1-3} requires an E^* of about 140 eV. The measured inelastic losses ΔE_{1-2} and ΔE_{1-3} are therefore in excellent agreement with the promotion of one and two Li 1s electrons, respectively, to empty states near the Fermi level during a single collision.

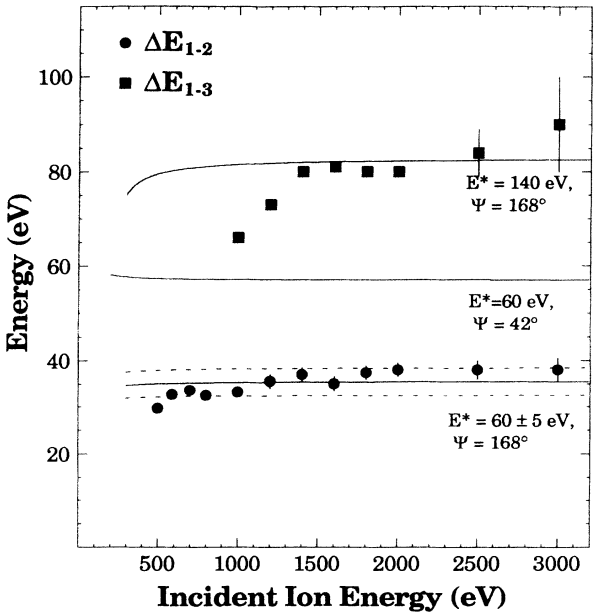

FIG. 12. Peak separation ΔE_{1-2} (●) and ΔE_{1-3} (■) as a function of E_0 shown along with inelastic losses calculated using Eq. (3) for the various values of E^* and Ψ as indicated.

The idea that the magnitude of the discrete loss of the projectile depends on the scattering angle is helpful in interpreting the ion scattering spectra collected at $\Psi = 42°$. For $E^* = 60$ eV, and $\Psi = 42°$, the predicted inelastic loss for a ^{7}Li projectile scattered from ^{27}Al is ~ 57 eV, as shown in Fig. 12. The Al SSP for $E_0 = 1.0$ keV and $\Psi = 42°$, as shown in Figs. 3 and 10(c), is sufficiently narrow and isolated that it would be resolved from a 57-eV loss feature. Since no loss feature is evident in the data, the incident energy threshold for the Li 1s electron promotion for a $\Psi = 42°$ scattering event must be greater than 1.0 keV. This can be compared to the threshold of ~ 0.5 keV observed for $\Psi = 168°$.

The association of a higher promotion threshold with a smaller Ψ reflects the fact that the distance of closest approach increases with decreasing Ψ for a given E_0. To illustrate this, the distance of closest approach for binary Li-Al collisions was calculated for $\Psi = 168°$ and 42° for several values of E_0 using the Thomas-Fermi-Molière potential with the screening length modified by a factor of $c = 0.8$. The results of these calculations are plotted in Fig. 13. The distance of closest approach for the onset energy of P2, $E_0 = 0.5$ keV, in the $\Psi = 168°$ configuration is 0.68 Å, which can be used to approximate r_c. The closest approach for $E_0 = 1.0$ keV, $\Psi = 42°$, is 0.67 Å, which is just within the approximated r_c. It is therefore reasonable, within the context of the MO model, that there is no prominent loss feature in the $E_0 = 1.0$ keV, $\Psi = 42°$ spectrum.

The creation of a Li 1s hole is the first step in the formation of Li*($1s2s^2$). The presence of Li*($1s2s^2$) is detected in the electron emission spectra as it deexcites via the intra-atomic Auger autoionization process

$$\mathrm{Li}^*(1s2s^2) \rightarrow \mathrm{Li}^+(1s^2) + e^- ,$$

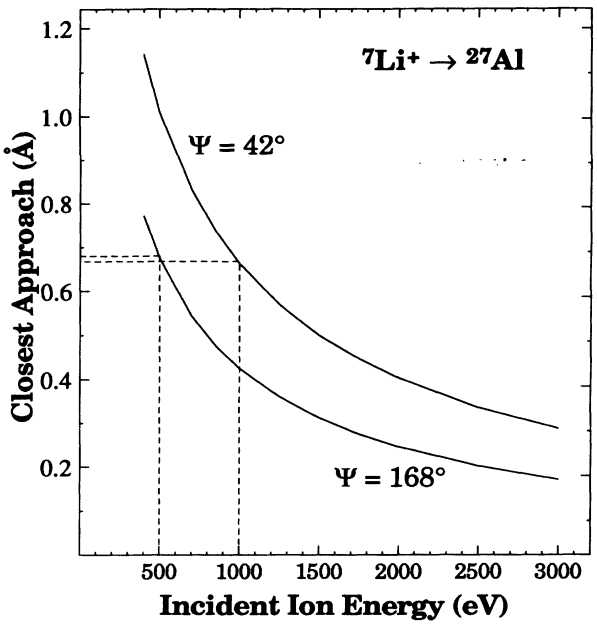

FIG. 13. Calculated values for the distance of closest approach during binary Li-Al collisions for $\Psi=168°$ and $\Psi=42°$ shown as a function of E_0.

where the ejected e^- leaves the Li 2s level with a characteristic energy. Studies of atomic collisions show that the energy of the ejected electron is 50.9 eV in the rest frame of the Li particle.[58,59] In Ref. 46, a Li AU(1,2) peak is seen 51 eV above the low-energy cutoff in spectra of secondary electrons collected near the surface normal with a grazing 2-keV Li^+ beam impinging on a Li-covered W(100) surface. In the spectra of the electron emissions shown in Fig. 9, the Li AU(1,2) peaks produced at lower incident Li^+ energies are at 51 eV, in excellent agreement with the deexcitation of $Li^*(1s2s^2)$. At higher energies, however, the velocities of the excited particles increase, causing significant Doppler shifts. It is interesting to note that there is no apparent emission due to the autoionization of higher Li* states. For example, the two configurations of $Li^*(1s2s2p)$ eject 53.5 and 55.0-eV electrons and $Li^*(1s2p^2)$ emits a 55.6-eV electron.

Autoionization of the $Li^*(1s2s^2)$ state also explains the distinct response of the P2 signal to alkali adsorption, as seen in Fig. 8. With one less electron to shield the nucleus, the 2s level is more tightly bound than in the ground state, i.e., the binding energy is 16 eV instead of 5.39 eV.[56] The lower-lying 2s level thus has a large overlap with the Al conduction band, and consequently a very high probability of being doubly occupied, i.e., forming $Li^*(1s2s^2)$, as it leaves the surface. Then, after $Li^*(1s2s^2)$ escapes the surface, it autoionizes. Since singly scattered ^7Li in the present study travels away from the surface at a rate between 0.7 and 2.2 Å/fs, and the mean lifetime of $Li^*(1s2s^2)$ is on the order of 18 fs,[60] it is reasonable to expect that $Li^*(1s2s^2)$ typically travels 10 to 40 Å away from the surface before autoionizing. This is far enough above the surface to inhibit resonant neutralization of the resulting ground-state Li^+ ions.

It is interesting to compare the behavior of P3 to that of P2. P3 is like P2 in that it is resistant to the increased resonant neutralization associated with alkali adsorption, which is an indication that autoionization is actively contributing to the P3 ion yield. On the other hand, the electron emission spectra show no features corresponding to the autoionization of a Li** species with a double Li 1s hole, such as $Li^{**}(2s^22p)$ which is characterized by 71-eV electron emissions.[57] This means either that double Li 1s holes are so short-lived that it is very unlikely that they escape the surface, or that some other excitation is responsible for P3.

There are, however, rather severe restrictions on the possible excitations that might produce P3. First, the excitation must initiate the formation of an autoionizing Li state to account for the response of the neutralization behavior of P3 to alkali adsorption. Since there are no other autoionization features observed, the excitation must therefore involve the production of $Li^*(1s2s^2)$. Second, all of the inelastic losses responsible for P3 must occur during a single collision. The second restriction holds because sequential excitations would not produce a sharp loss feature correlated to a SSP. To the extent that sequential excitations do occur, they happen during the course of many different combinations of scattering events. Because both the elastic energy loss and the partitioning of the inelastic loss between the projectile and the target atoms vary greatly for different collision combinations, the total energy loss experienced by projectiles after two or more inelastic collisions would not be as well defined as is P3. The excitation must also have a total E^* of $\sim$140 eV to be consistent with the separation of P3 from P1. Therefore, the most likely cause for P3 is the simultaneous excitation of two Li 1s electrons followed by the rapid filling of one of the vacancies before escaping the surface.

Assuming that P3 is a consequence of the simultaneous promotion of two Li 1s electrons, there are several reasons why a double 1s hole would have a shorter lifetime than a single 1s hole. Because the double hole is lower in energy than the single hole, more deexcitation channels are available to partially fill empty Li 1s levels. For example, the empty Li 1s level is sufficiently below the Al 2p level to open an Auger decay channel, i.e., an Al 2p electron fills one of the empty Li 1s states and releases enough energy to lift another electron above the Fermi level. The singly occupied Li 1s level, on the other hand, is located above the 73-eV Al 2p level and therefore cannot be filled by Al 2p electrons. Although it may be coincidental, the Al LMM peak begins to emerge at 1.0 keV, which is about the same as the threshold incident energy for P3. While most of the AL LMM signal is probably produced during ion-induced collision cascades, some of the signal may be due to the decay of Al 2p holes created via the filling of vacant Li 1s levels.

There are several indications in the scattered ion spectra collected from alkali-covered surfaces that, as predicted by the correlation diagrams in Fig. 11, Li 1s promotions take place only during Li-Al collisions and not during Li-Na or Li-K collisions. First of all, as shown in

Fig. 7, the inelastic loss experienced by Li^+ singly scattered from K tracks very closely with P1, indicating that Li^+ scattered from K experiences only the usual continuous inelastic losses. If Li 1s promotions with $E^*=60$ eV were occurring during Li-K or Li-Na collisions, then according to Eq. (3), the Li would undergo additional discrete inelastic losses of 32 and 42 eV, respectively. Clearly, this is not the case for the K SSP. Furthermore, the Na SSP and K SSP intensities are small compared to P2, suggesting that the measured ion yields at the Na and K SSP energies are not enhanced by autoionization.

Consideration of the specific example of the spectrum shown in Fig. 5(b) for scattering of 3-keV Li^+ from the 0.5-ML Na/Al(100)-$c(2\times2)$ surface makes it clear that the measured charge state of singly scattered Li^+ is dependent on the scattering site. In the absence of neutralization, the intensity of the Na SSP at the $c(2\times2)$ coverage would be nearly $\frac{1}{3}$ of the Al SSP for the following reasons: At normal incidence on an fcc (100) surface, the first two atomic layers are directly visible to the incident ion beam, while deeper layers are shadowed. Thus, the first two atomic layers are responsible for all of the observed single scattering signal from the clean surface. At the 0.5-ML $c(2\times2)$ coverage, however, for any simple adsorption geometry, half of ML of Al atoms would be shadowed by Na, so that there would be 1.5 ML of Al atoms and 0.5 ML of Na visible to the incoming beam. This three-to-one ratio of Al to Na targets is nearly representative of the single scattering probabilities and only slightly modified by scattering cross sections, as the ratio of the partial cross sections for 3-keV $^7Li^+$ to scatter through 168° from Na, as compared to Al, is 0.89. Thus, the fact that the Na SSP is much smaller than $\frac{1}{3}$ of the Al SSP demonstrates that singly scattered Li is more likely to reach the analyzer as a neutral when scattered from Na than from Al. The chemical selectivity of electron promotions predicted by the quasimolecular model is also borne out by other experiments on composite surfaces. For example, reionization of He scattered from InP occurs only during He-In collision,[40] and $Ne^{**}(2p^43s^2)$ states are generated only by Ne-Mg collisions at MgO surfaces[43] and Ne-Cu collisions at $Cu_3Au(100)$.[44]

The above interpretation accounts for the main features of the present results. The inelastic losses in the ion scattering spectra are due to the promotion of Li 1s electrons to empty states above the Fermi level. Loss features are not seen in scattering from Na or K because Li-Na and Li-K molecular states do not mediate Li 1s promotions. A consequence of the Li 1s promotions is the formation of autoionizing $Li^*(1s2s^2)$ states which are, in turn, responsible for the Li AU(1,2) electron emissions as well as for the resistance of the ion scattering loss features to alkali-induced resonant neutralization. Closer examination of the data, however, yields some additional details which further characterize the electronic processes that occur in this system.

One thing to consider is that the data points for ΔE_{1-2} and ΔE_{1-3} do not precisely follow the excitation energy contours for Q_p as a function of E_0 shown in Fig. 12. One difference is that ΔE_{1-2} and ΔE_{1-3} increase somewhat more rapidly as a function of E_0 than the free atom model represented by Eq. (3) predicts. Another difference is that, at the onset energies of P2 and P3, the data for ΔE_{1-2} and ΔE_{1-3} fall below the contours for E^* that represent the excitation of a Li 1s electron to the lowest-lying empty state. Taken at face value, it would appear that Li 1s electrons were being promoted into states below the Fermi level. These discrepancies can be accounted for, however, if the effects of the dissipative inelastic energy losses and the energy dependence of the electron promotion probability are considered.

The rate at which ΔE_{1-2} and ΔE_{1-3} increase as a function of E_0 is, in part, due to the different continuous inelastic losses experienced by Li* particles with 1s holes and ground-state Li as they travel through the surface region. The energy dissipated per distance traveled depends not only on the speed of the projectile, but also on its charge state. After losing a 1s electron, the Li nucleus is less screened, resulting in a stronger Coulombic interaction between the Li projectile and the crystal. Excited $Li^*(1s2s^2)$ particles therefore experience larger dissipative forces than their ground-state counterparts. Because the energy dissipated via the Coulombic interaction also increases with the speed of the projectile,[61] the additional continuous energy loss caused by the 1s hole becomes more significant at higher energies. Thus, ΔE_{1-2} and ΔE_{1-3} increase more rapidly with E_0 than the calculated inelastic loss.

The reason behind the apparent discrepancies between the values of ΔE_{1-2} and ΔE_{1-3} near the threshold and the minimal amount of energy required to promote Li 1s electrons is that, near the onset of the excitation, the difference between the peak centers is not an accurate reflection of the discrete inelastic loss. At the onsets of P2 and P3, promotion probabilities are rapidly increasing as a function of E_0. This is evident in Fig. 8, where the intensity of P2 relative to P1 increases rapidly with E_0 near the threshold energy for P2. Because singly scattered particles experience different amounts of inelastic loss prior to the collision, there will be a distribution of collision energies. Near the threshold, Li particles at the higher end of the collision energy distribution are more likely to undergo Li 1s promotions than those at the lower end of the distribution since they will experience a smaller distance of closest approach. The net effect is that the discrete inelastic loss associated with the promotion preferentially reduces the higher side of P1 and augments the higher side of P2, so that the separation between P1 and P2 is smaller than the inelastic loss. The effect is even greater for ΔE_{1-3} than for ΔE_{1-2} because the collision energy distribution is broader at the higher threshold energy associated with P3.

The electron emission data compliment the results of the ion scattering data in a number of ways. One was is that the electron emission spectra sample a different population of the excited Li* than the ion scattering spectra, as the $Li^*(1s2s^2)$ particles responsible for the Li AU(1,2) signal are not necessarily traveling toward the analyzer. This is why $Li^*(1s2s^2)$ emissions can be detected in the

$\Psi=42°$ configuration with E_0 as low as 0.5 keV, even though this is well below the threshold for the Li 1*s* promotions for scattering at that angle. Likewise, the small, but unmistakable, Li AU(1,2) signal produced by the 0.4-keV beam in Fig. 9(a) shows that the absolute threshold for the Li 1*s* promotion is actually ~400 eV or less, even though the ion scattering data collected at $\Psi=168°$ show no evidence of electron promotions when $E_0=0.4$ keV.

Additional information about the excited-state population can be obtained by analyzing the Doppler shifts in the Li AU(1,2) signal. The magnitude of the Doppler shift expected for the spectra in Fig. 9(a) can be quickly estimated by assuming that the typical velocity of the deexciting Li* in the direction of the analyzer is well represented by the velocity of the ions contributing to P2. The final energy of the electrons from these sources can then be calculated using a simple Galilean transformation. This approximation locates the Li AU(1,2) peak at 52.5 eV for the 0.5-keV spectra and 56.2 eV for the 5-keV spectra. The 3.7-eV relative shift predicted by this calculation is only slightly larger than the observed shift of ~2.5 eV. The agreement is actually quite good, considering the simplicity of the approximation.

The same reasoning cannot be directly applied to the Doppler shifts seen in the emission spectra in Fig. 9(b), however, because the loss features were not isolated and identified in the corresponding ion scattering spectra collected at $\Psi=42°$. However, the fact that the Li AU(1,2) peak shifts to higher energy as E_0 increases indicates that Li 1*s* promotions do occur during forward-scattering events. After all, if Li 1*s* holes were only being formed during backscattering events, the Li* velocity distribution would be directly away from the analyzer and only negative Doppler shifts would be seen. Contrary to this, the Li AU(1,2) peak shifts measurably toward higher energy when $E_0=1.0$ keV and shifts dramatically by $E_0=3.0$ keV, indicating that promotions begin to occur for forward scattering by ~1.0 keV. Because cross sections for forward scattering are much higher than the cross sections for backscattering, many of the electron promotions may occur during grazing collisions when E_0 is on the order of a few keV.

Given that electron promotions do occur during forward scattering at higher incident energies, it is not surprising that the Doppler shifts are larger for the spectra in Fig. 9(b) than in Fig. 9(a), as the forward-scattered particles lose less energy than those that are backscattered. The energy loss experienced by $^7Li^+$ from Al is over 65% for $\Psi=168°$, but only about 13% for $\Psi=42°$. In the two cases where $\Psi=42°$, the average component of the velocity distribution of the excited particles in the direction toward the analyzer is larger when $\Theta=\Theta_{SFP}$ than when $\Theta=30°$ for the following reasons: As seen in the Monte Carlo simulation shown in Fig. 10(c), when an ion beam is incident along $\Theta=\Theta_{SFP}$ in the [011] plane of a fcc (100) surface, the vast majority of the scattering events are grazing collisions from the first two atomic layers. On the other hand, for $\Theta=30°$, the ions penetrate deeper into the crystal and experience more multiple collisions, thereby reducing the average component of the velocity distribution of the excited particles in the direction of the analyzer. The measured shifts in the Li AU(1,2) peak produced with the beam at $\Theta=\Theta_{SFP}$ are 2, 5, and 7 eV for $E_0=1$, 3, and 5 keV, respectively. Assuming that the velocity distribution in this configuration is reasonably well characterized by the BCM energy for ^7Li scattering into the analyzer at $\Psi=42°$, the calculated Doppler shifts of 3.8, 6.6, and 8.7 eV, respectively, compare very well with the data. The abrupt shift in the Li AU(1,2) position between 1 and 3 keV also suggests that the number of promotions occurring in the forward-scattering direction increases rapidly during this interval.

V. SUMMARY

Spectra of the scattered ions and the ion-induced electron emissions provide useful information for understanding collision-induced electronic processes. The present study employed both techniques for low-energy (0.4–5 keV) $^7Li^+$ ions scattering from Al(100), Na/Al(100), and K/Al(100). The complementary ion scattering and secondary electron data provide sufficient information to detail a process in which inner-shell electrons are promoted from the incident ions to states just above the Fermi level of the solid. For scattering from the alkali-atom-covered surfaces, Li 1*s* promotion occurs only during Li-Al collisions and not during Li-Na or Li-K collisions. As a result, discrete inelastic losses and increases in the ion yield via autoionization are associated with single scattering from Al.

ACKNOWLEDGMENTS

This work was supported by the Director, Office of Energy Research, Office of Basic Energy Sciences, Materials Sciences Division of the U. S. Department of Energy under Contract No. DE-AC03-76SF00098.

*Present address: Battelle Pacific Northwest Laboratories, P.O. Box 999, Richland, WA 99352.

[1]W. Heiland and A. Närmann, Nucl. Instrum. Methods Phys. Res. Sect. B **78**, 20 (1993).
[2]J. Los and J. J. C. Geerlings, Phys. Rep. **190**, 133 (1990).
[3]J. B. Marston, D. R. Andersson, E. R. Behringer, and B. H. Cooper, Phys. Rev. B **48**, 7809 (1993).
[4]S. Valeri, Surf. Sci. Rep. **17**, 85 (1993).
[5]R. A. Baragiola, Nucl. Instrum. Methods Phys. Res. Sect. B **78**, 223 (1993).
[6]Th. Fauster, Vacuum **38**, 129 (1988).
[7]H. Niehus and G. Comsa, Surf. Sci. **140**, 18 (1984).
[8]A. J. Algra, E. van Loenen, E. P. Th. M. Suurmeijer, and A. L. Boers, Radiat. Effects **60**, 173 (1982).
[9]T. M. Buck, G. H. Wheatley, and L. K. Verheij, Surf. Sci. **90**, 635 (1979).

[10]M. J. Ashwin and D. P. Woodruff, Surf. Sci. **244**, 247 (1991).
[11]M. Beckschulte and E. Taglauer, Nucl. Instrum. Methods Phys. Res. Sect. B **78**, 29 (1993).
[12]K. A. H. German, C. B. Weare, P. R. Varekamp, J. N. Andersen, and J. A. Yarmoff, Phys. Rev. Lett. **70**, 3510 (1993).
[13]G. A. Kimmel and B. H. Cooper, Phys. Rev. B **48**, 12 164 (1993).
[14]L. Jiang, Y. D. Li, and B. E. Koel, Phys. Rev. Lett. **70**, 2649 (1993).
[15]J. J. C. Geerlings, L. F. T. Kwakman, and J. Los, Surf. Sci. **184**, 305 (1987).
[16]G. A. Kimmel, D. M. Goodstein, and B. H. Cooper, J. Vac. Sci. Technol. A **7**, 2186 (1989).
[17]G. A. Kimmel, D. M. Goodstein, Z. H. Levine, and B. H. Cooper, Phys. Rev. B **43**, 9403 (1991).
[18]E. R. Behringer, D. R. Andersson, D. M. Goodstein, B. Kasemo, and B. H. Cooper, Nucl. Instrum. Methods Phys. Res. Sect. B **78**, 3 (1993).
[19]C. B. Weare, K. A. H. German, and J. A. Yarmoff (unpublished).
[20]G. Ertl, in *Physics and Chemistry of Alkali Metal Adsorption,* edited by H. P. Bonzel, A. M. Bradshaw, and G. Ertl (Elsevier, Amsterdam, 1989).
[21]T. Aruga and Y. Murata, Prog. Surf. Sci. **31**, 61 (1989).
[22]K. A. H. German, C. B. Weare, and J. A. Yarmoff, Phys. Rev. Lett. **72**, 3899 (1994).
[23]A. Schmalz, S. Aminpirooz, L. Becker, J. Haase, J. Neugebauer, M. Scheffler, D. R. Batchelor, D. L. Adams, and E. Bøgh, Phys. Rev. Lett. **67**, 2163 (1991).
[24]S. Aminpirooz, A. Schmalz, L. Becker, N. Pangher, J. Haase, M. M. Nielsen, D. R. Batchelor, E. Bøgh, and D. L. Adams, Phys. Rev. B **46**, 15 594 (1992).
[25]J. N. Andersen, M. Qvarford, R. Nyholm, J. F. v. Acker, and E. Lundgren, Phys. Rev. Lett. **68**, 94 (1992).
[26]J. N. Andersen, E. Lundgren, R. Nyholm, and M. Qvarford, Phys. Rev. B **46**, 12 784 (1992).
[27]J. N. Andersen, E. Lundgren, R. Nyholm, and M. Qvarford, Surf. Sci. **289**, 307 (1993).
[28]A. Schmalz, S. Aminpirooz, L. Becker, J. Haase, D. R. Batchelor, D. L. Adams, and E. Bøgh, Surf. Sci. **269/270**, 659 (1992).
[29]A. Schmalz, S. Aminpirooz, J. Haase, D. R. Batchelor, M. M. Nielsen, E. Bøgh, and D. L. Adams, Surf. Sci. **301**, L211 (1994).
[30]C. Stampfl, M. Scheffler, H. Over, J. Burchhardt, M. Nielsen, D. L. Adams, and W. Moritz, Phys. Rev. Lett. **69**, 1532 (1992).
[31]C. Stampfl, J. Burchhardt, M. Nielsen, D. L. Adams, M. Scheffler, H. Over, and W. Mortiz, Surf. Sci. **287/288**, 418 (1993).
[32]C. Stampfl, M. Scheffler, H. Over, J. Burchhardt, M. Nielsen, D. L. Adams, and W. Moritz, Phys. Rev. B **49**, 4959 (1994).
[33]R. Souda, T. Aizawa, C. Oshima, and Y. Ishizawa, Nucl. Instrum. Methods Phys. Res. Sect. B **45**, 364 (1990).
[34]F. Shoji, K. Oura, and T. Hanawa, Surf. Sci. **205**, L787 (1988).
[35]R. Souda, T. Aizawa, C. Oshima, M. Aono, S. Tsuneyuki, and M. Tsukada, Surf. Sci. **187**, L592 (1987).
[36]M. Aono and R. Souda, Nucl. Instrum. Methods Phys. Res. Sect. B **27**, 55 (1987).
[37]R. Souda, T. Aizawa, S. Otani, and Y. Ishizawa, Surf. Sci. **232**, 219 (1990).
[38]R. Souda, M. Aono, C. Oshima, S. Otani, and Y. Ishizawa, Surf. Sci. **150**, L59 (1985).
[39]F. Shoji, Y. Nakayama, and T. Hanawa, Surf. Sci. **163**, L745 (1985).
[40]F. Shoji, K. Kashihara, T. Hanawa, and K. Oura, Nucl. Instrum. Methods Phys. Res. Sect. B **47**, 1 (1990).
[41]R. Souda and M. Aono, Nucl. Instrum. Methods Phys. Res. Sect. B **15**, 114 (1986).
[42]R. Souda, T. Aizawa, C. Oshima, S. Otani, and Y. Ishizawa, Phys. Rev. B **40**, 4119 (1989).
[43]O. Grizzi, M. Shi, H. Bu, and J. W. Rabalais, Phys. Rev. B **41**, 4789 (1990).
[44]T. M. Buck, W. E. Wallace, R. A. Baragiola, G. H. Wheatley, J. B. Rothman, R. J. Gorte, and J. G. Tittensor, Phys. Rev. B **48**, 774 (1993).
[45]I. Terzic, D. Ciric, and N. Neskovic, Radiat. Effects **54**, 177 (1981).
[46]H. Brenten, H. Müller, and V. Kempter, Z. Phys. D **22**, 563 (1992).
[47]C. Benazeth, P. Cafarelli, and N. Benazeth, Nucl. Instrum. Methods Phys. Res. Sect. B **62**, 47 (1991).
[48]I. Terzic, M. Tosic, and Z. Radocevic, J. Vac. Sci. Technol. A **10**, 3359 (1992).
[49]I. Terzic, Z. Radocevic, and M. Tosic, Surf. Sci. **260**, 200 (1992).
[50]J. A. Yarmoff and R. S. Williams, Surf. Sci. **165**, L73 (1986).
[51]J. Paul, J. Vac. Sci. Technol. A **5**, 664 (1987).
[52]J. Fine, M. Szymonsk, J. Kolodziej, M. Yoshitake, and K. Franzreb, Phys. Rev. Lett. **71**, 3585 (1993).
[53]G. Zampieri and R. Baragiola, Phys. Rev. B **29**, 1480 (1984).
[54]J. A. Yarmoff and R. S. Williams, Surf. Sci. **127**, 461 (1983).
[55]M. Barat and W. Litchen, Phys. Rev. A **6**, 211 (1972).
[56]C. E. Moore, *Atomic Energy Levels,* Natl. Bur. Stand. U.S. Circ. No. 467 (U.S. GPO, Washington, DC, 1971), Vol. 1.
[57]R. Bruch, G. Paul, and J. Andrä, Phys. Rev. A **12**, 1808 (1975).
[58]M. Rødbro, R. Bruch, and P. Bisgaard, J. Phys. B **12**, 2413 (1979).
[59]D. J. Pegg, H. H. Haselton, R. S. Thoe, P. M. Griffin, M. D. Brown, and I. A. Sellin, Phys. Rev. A **12**, 1330 (1975).
[60]B. F. Davis and K. T. Chung, Phys. Rev. A **31**, 3017 (1985).
[61]A. Närmann, W. Heiland, R. Moneal, F. Flores, and P. M. Echenque, Phys. Rev. B **44**, 2003 (1991).

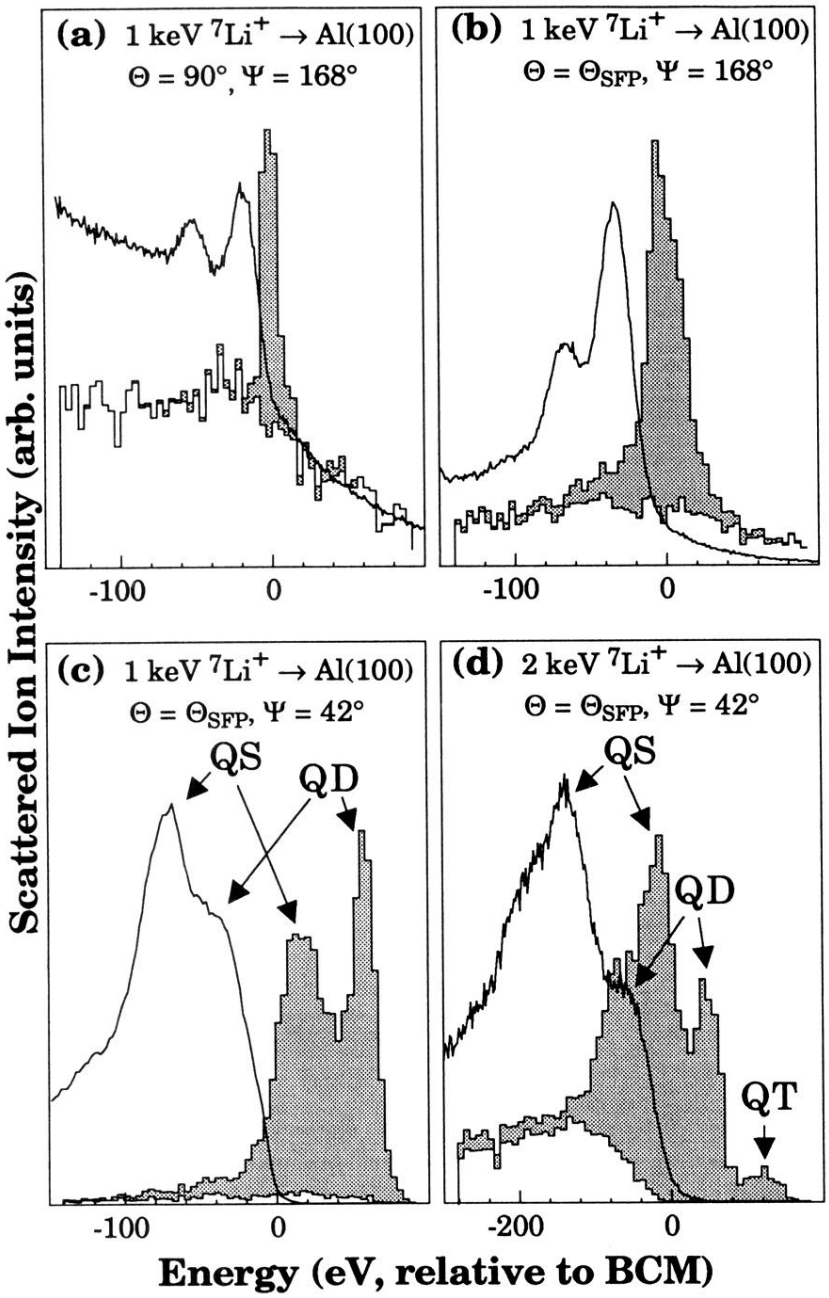

FIG. 10. Monte Carlo simulations of $^7Li^+$ ion scattering spectra for (a) $E_0 = 1$ keV, $\Psi = 168°$, $\Theta = 90°$; (b) $E_0 = 1$ keV, $\Psi = 168°$, $\Theta = \Theta_{SFP} = 22°$, (c) $E_0 = 1$ keV, $\Psi = 42°$, and $\Theta = \Theta_{SFP} = 22°$, and (d) $E_0 = 2$ keV, $\Psi = 42°$, and $\Theta = \Theta_{SFP} = 19°$. The histograms are divided into surface events (gray) and subsurface events (white), according to whether or not the trajectory extended past the first two atomic layers. The corresponding experimental data are superimposed on each panel. The intensities of the simulation and the experimental data are arbitrarily scaled to each other.